Yttrium-based Double Perovskite Nanorods for Electrocatalysis

Scott C. McGuire[1], Weiqiao Wesley[1], Kotaro Sasaki[2], Xiao Tong[3], and

Stanislaus S. Wong[1,*]

Email: stanislaus.wong@stonybrook.edu

[1]Department of Chemistry, State University of New York at Stony Brook,

Stony Brook, NY 11794-3400

[2]Chemistry Division, Brookhaven National Laboratory, Building 555,

Upton, NY 11973

[3]Center for Functional Nanomaterials, Building 735,

Brookhaven National Laboratory, Upton, NY 11973

Abstract. Herein, we investigate the effect of chemical composition of double perovskite nanorods on their versatile electrocatalytic activity not only as supports for the oxidation of small organic molecules but also as catalysts for the oxygen evolution reaction. Specifically, Y_2CoMnO_6 and Y_2NiMnO_6 nanorods with average diameters of 300 nm were prepared by a two-step hydrothermal method, in which the individual effects of synthetic parameters, such as the pH, annealing temperature, and precursor ratios on both the composition and morphology, were systematically investigated. When used as supports for Pt nanoparticles, Y_2CoMnO_6/Pt catalysts exhibited an electrocatalytic activity for the methanol oxidation reaction, which is 2.1 and 1.3 times higher than that measured for commercial Pt/C and Y_2NiMnO_6/Pt. Similarly, the Co-based catalyst support material displayed an ethanol oxidation activity, which is 2.3 times higher than both Pt/C and Y_2NiMnO_6/Pt. This clear enhancement in the activity for Y_2CoMnO_6 can largely be attributed to strong metal-support interactions, as evidenced by a downshift in the binding energy of the Pt 4*f* bands, measured by XPS, which is often correlated not only with a downshift in the *d*-band center but also to a decreased adsorption of poisoning adsorbates. Moreover, when used as catalysts for the oxygen evolution reaction, Y_2CoMnO_6 displayed a much greater activity as compared with Y_2NiMnO_6. This behavior can largely be attributed not only to a preponderance of comparatively more favorable oxidation states and electronic configurations but also to the formation of an active layer on the surface of the Y_2CoMnO_6 catalyst, which collectively give rise to improved performance metrics and greater stability as compared with both IrO_2 and Y_2NiMnO_6. Overall, these results highlight the importance of both the chemical composition and the electronic structure of double perovskites, especially when utilized in multi-functional roles as either supports or catalysts.

Keywords: double perovskites, nanorods, catalysis, supports, electrocatalysis

Introduction

The use of precious metals underlies the majority of current state-of-the-art catalysts for various electrocatalytic reactions, including but not limited to the oxidation of small organic molecules (SOMs), the oxygen evolution reaction (OER), and the oxygen reduction reaction (ORR). However, Pt-based systems in particular are limited in use by their high cost and poor stability. As such, research has focused on the development of alternative electrocatalysts, such as metal oxides, which have shown promising results as both supports and active catalysts.

As an illustrative example, transition-metal-based perovskite oxides with a general formula of ABO_3, wherein 'A' is either an alkaline, alkaline-earth, or rare-earth metal and 'B' denotes a d-block transition metal, have been probed for a wide array of applications, such as but not limited to electrocatalysis,[1] photovoltaics,[2] photocatalysis,[3] and energy storage.[4-6] Specifically, this class of materials has shown considerable promise as both active catalysts for OER and ORR, in addition to as support materials for Pt nanoparticles in the context of methanol and ethanol oxidation reactions (MOR/EOR), due to their low cost, high stability, compositional tunability, and overall favorable performance.[7] Moreover, substituting the A- and B-sites within perovskites can be used to easily tailor their physical and chemical properties. In fact, by partial substitution at the B-site, double perovskites possessing the formula of $A_2BB'O_6$ can be generated, which can allow for a high degree of tunable compositional control as compared with the single ABO_3 perovskite structure alone. By analogy with single perovskites, double perovskites have demonstrated promise for many applications, including electrocatalysis.[8]

Specifically, double perovskites have been reported as intriguing candidates for OER and ORR electrocatalysts, wherein the activity can be systematically modified by carefully varying the composition. For example, the activity of La_2NiMnO_6 could be increased by controlling the

valence states of Mn and Ni.[9] It was noted that as the oxidation state is altered from Mn^{4+}-O-Ni^{2+} to Mn^{3+}-O-Ni^{3+}, the current density for OER at a specific overpotential of 500 mV increased from 14.19 mA cm^{-2} to 101.8 mA cm^{-2}, wherein the change in oxidation states induced a strong Jahn-Teller distortion of the BO_6 octahedra and an apparent elongation of the metal-oxygen bonds, all of which can facilitate the formation of active species at the outer surfaces of the catalysts. Similarly, a study of La_2NiMnO_6 and La_2CoMnO_6 indicated that the degree of e_g orbital occupation, related to the oxidation states of the constituent B-site metals, has a direct correlation with the measured activity for both OER and ORR.[10] To account for these observations in part, a crucial predictor for the OER/ORR activity of a transition metal oxide is the difference between the metal *d*-band center and the oxygen 2*p* band center (ΔE_{d-p});[11] increasing the transition metal-oxygen 'covalency' with a greater spatial overlap of electronic states promotes favorable charge transfer.[12, 13] For ABO_3 perovskites,[14] σ*-antibonding (e_g) orbital filling of the B site close to 1 leads to high OER activity.

Indeed, the physicochemical properties and electrocatalytic activity of perovskites are fundamentally dictated by the nature of the chemical substitution at the A- and B-sites, which impact the observed valence states and associated quantity of oxygen vacancies, all of which can affect performance.[15] For example, $LaMn_{0.3}Co_{0.7}O_3$ was reported to exhibit an enhanced halfwave potential of 0.72 V for ORR, which is 52 mV higher than that of $LaCoO_3$.[16] Moreover, $LaMn_{0.3}Co_{0.7}O_3$ also demonstrated a reduced OER overpotential of 416 mV, which is 64 mV lower than that of $LaCoO_3$. This enhancement in both OER and ORR performance is largely attributed to the optimization of the Co-O bond covalency and a concomitant reduction of the e_g orbital-filling from 1.23 for $LaCoO_3$ to 1.02 in $LaMn_{0.3}Co_{0.7}O_3$.

For the electrooxidation of SOMs, previous metal electrocatalysts are typically deposited onto an underlying support so as to not only prevent the aggregation of the catalyst nanoparticles but also slow the ripening process. Perovskite oxides have been proposed as alternatives to commercial carbon black supports, due to their ability to generate strong metal-support interactions (SMSIs) which can enable the perovskites to behave as effective co-catalysts.[17, 18] Electronic metal−support interactions (EMSIs) have been suggested as a means of modulating the catalyst metal's *d*-band centers (through a beneficial upshift relative to the Fermi level) to achieve outstanding catalytic activity.[19] In general, these effects can manifest as either changes in the lattice parameters of the catalyst, charge transfer between the support and catalyst, or a combination of both.

Moreover, perovskite oxides exhibit an increased electrochemical stability as compared with carbon supports, a finding which can partially be attributed to their ability to facilitate the oxidation and removal of deleterious poisoning intermediates from the surface of the Pt catalysts. Similar to that for OER/ORR, the performance of perovskite oxides as support materials for the oxidation of SOMs can be reliably tuned by controlling the oxidation states of the metals and the degree of substitution at either the A- or B-site with implications for the associated number of available oxygen vacancies. Indeed, the oxygen vacancy distribution can be modulated by means of anion defects, cation substitution, and ion non-stoichiometry.[20, 21] A higher O 2*p* band center relative to the Fermi level leads to a smaller energy penalty to form oxygen vacancies.[21]

While most work for MOR or EOR has focused on single perovskites, our group has recently reported that the observed activity is correlated with chemical composition. In fact, we noted that Ni-containing perovskites, such as $LaNiO_3$ and La_2NiMnO_6, were able to achieve comparable activities for MOR and outperformed both $LaMnO_3$ and the Pt/C standard, when

these lanthanum-based perovskites were used as supports for Pt nanoparticles.[22] Interestingly, we also observed that anisotropic nanorods achieved a noticeably higher MOR performance as compared with nanocubes possessing a similar size, all else being equal.

Indeed, the morphology of not only the underlying catalyst support for SOM oxidation but also the catalyst for OER can have a significant impact upon the resulting electrocatalytic performance.[23] In the context of both MOR and EOR, Pt/MnO_2/C composites, incorporating MnO_2 nanorods, achieved perceptibly higher activities as compared with their nanocube counterparts.[24] This observed increase in activity was largely attributed to a corresponding increase in the active surface area available, associated with the interface encompassing Pt, the MnO_2 nanorod, and the electrolyte. This favorable geometrical configuration enabled a better adsorption of oxidizing species, which could assist in removing poisoning species, such as CO. As a different example for OER, it was noted that $La_{0.8}Sr_{0.2}Co_{0.2}Fe_{0.8}O_{3-\delta}$ 1D nanofibers could achieve a current density of 10 mA cm^{-2} at 1.643 V, which is 59 mV lower than that for analogous nanoparticles.[25]

Herein, to capitalize on the electrocatalytic value of anisotropic motifs, we report on the synthesis of Y_2NiMnO_6 (YNMO) and Y_2CoMnO_6 (YCMO) nanorods and their performance as not only catalysts for OER and ORR but also supports for Pt nanoparticles in the electrooxidation of methanol and ethanol. To the best of our knowledge, this is the first report in which Y-based double perovskites have been successfully used in dual roles, functioning as either supports or catalysts for the oxidation of SOMs and OER/ORR, respectively. The crystallinity, structure, morphology, and composition of the as-prepared perovskite nanorods were confirmed by a number of characterization methods, including X-ray diffraction (XRD), scanning electron microscopy (SEM), transmission electron microscopy (TEM), and energy

dispersive X-ray spectroscopy (EDS). The surface chemistry of the as-generated nanorods was characterized by X-ray photoelectron spectroscopy (XPS) in order to provide insights into the catalytic activity.

Specifically, our results indicate that for the oxidation of SOMs, the chemical composition of the underlying perovskite support gives rise to a significant impact on the resulting metal-support interaction. In particular, YCMO nanorods maintained significantly superior performance for OER as compared with YNMO, achieving an overpotential of 590 mV, whereas YNMO yielded little if any measurable activity. This major difference in activity between the two perovskites can largely be explained by a difference in electronic configuration. That is, XPS measurements at the Mn 2*p* band indicate that YCMO consists entirely of Mn^{4+} and Co^{2+} species, which maintain an average e_g orbital occupation of one and can undergo vibronic superexchange, thereby forming a catalytically active layer at the surface. In addition, ORR measurements indicate that YCMO is can also act as a bifunctional catalyst

Experimental

Materials: The precursors and reagents, specifically yttrium nitrate hexahydrate (99.9%, Alfa Aesar), nickel nitrate hexahydrate (98%, Alfa Aesar), cobalt nitrate hexahydrate (need purity, Acros Organics), manganese acetate tetrahydrate (99.99%, Aldrich), sodium hydroxide (98.5%, Acros Organics), dihydrogen hexachloroplatinate(IV) hydrate (H_2PtCl_6, 99.9%, Alfa Aesar), sodium borohydride ($NaBH_4$, 99.99%, Alfa Aesar), and ethanol (denatured, BeanTown Chemical), were all used, as purchased.

Synthesis of Y_2NiMnO_6 (YNMO): In a typical synthesis, $Y(NO_3)_3$ (294 mg), $Ni(NO_3)_2$ (186 mg), and $Mn(acetate)_2$ (157 mg) were dissolved in 20 mL of water. Next, the pH was slowly adjusted

to the desired pH of 13.4 by the addition of 5 M NaOH. The solution was then transferred to a Teflon-lined stainless-steel autoclave and heated at 200°C for 24 h. The resulting intermediate was collected by centrifugation, washed with water and ethanol for several times, and then dried in an oven. The dry powder was subsequently annealed at 1000°C for 12 h, producing the desired double perovskite. The diameters of the nanorods could be reasonably controlled by carefully varying the pH value, prior to the hydrothermal reaction step.

Synthesis of Y_2CoMnO_6 (YCMO): In a typical synthesis, $Y(NO_3)_3$ (441 mg), $Co(NO_3)_2$ (186 mg), and $Mn(acetate)_2$ (157 mg) were dissolved in 20 mL of water. Next, the pH was slowly adjusted to the desired pH of 12.3 through the addition of 5 M NaOH. The solution was then transferred to a Teflon-lined stainless-steel autoclave and heated at 200°C for 24 h. The resulting intermediate was collected by centrifugation, washed with water and ethanol several times, and ultimately dried in an oven. Upon annealing at 1000°C for 4 h, the dry powder was converted to the desired double perovskite. The average diameters of the nanorods could be tuned by carefully modifying the pH reading, prior to the hydrothermal reaction step.

Deposition of Pt nanoparticles onto perovskite supports: As-prepared perovskites were dispersed into an aqueous solution of H_2PtCl_6, so as give rise to a final perovskite concentration of 1 mg/mL; that ended up being the minimum Pt concentration needed to achieve an overall mass loading of 20%. An aqueous solution of $NaBH_4$ (2 mg/mL) was later added to the perovskite dispersion, wherein 1 mL of the $NaBH_4$ solution was used per 2 mL of the perovskite dispersion; this mixture was allowed to stir for 30 min. The resulting product was collected by centrifugation and subsequently washed with water and ethanol for several times. The catalyst was finally dispersed in ethanol with a final concentration of 2 mg/mL.

Structural Characterization Techniques

Scanning electron microscopy: The as-prepared samples were dispersed in ethanol, prior to drop casting onto a *p*-doped silicon substrate. Microscopy images and associated morphological characterization data were obtained using both Hitachi S-4800 SEM and JEOL 7600 field emission SEM instruments.

Transmission electron microscopy: TEM samples were generated by dispersal in ethanol following by drop casting onto a lacey carbon-coated copper grid. TEM images were acquired using a JEOL JEM-1400 TEM instrument, equipped with a 2048 × 2048 Gatan CCD camera system and operated with an accelerating voltage of 120 kV. High resolution TEM (HRTEM) images were obtained with the assistance of a JEOL JEM-2100F TEM instrument with an acceleration voltage of 200 kV.

Powder X-ray diffraction: Samples were put together by dispersing in ethanol, followed by drop casting onto zero-background holders. Powder XRD patterns were collected using a Rigaku MiniFlex diffractometer, through the mediation of Cu Kα radiation ($\lambda = 1.54$ Å).

X-ray photoelectron spectroscopy: Samples were fabricated by immobilizing the product powders onto an underlying copper tape. These samples were subsequently placed into an ultrahigh vacuum chamber, characterized by a pressure of less than 5×10^{-9} Torr. XPS measurements were carried out using a home-built XPS surface analysis system, equipped with a hemi-spherical electron energy analyzer (SPECS, XR50). For the Co-based samples, an Al Kα (1486.61 eV) source radiation was utilized, whereas Ni-based samples were analyzed using Mg Kα (1253.6 eV) radiation. Both sets of materials were probed using current-voltage conditions of 13 kV and 30 mA, respectively. An angle of 45° was set between the analyzer and the X-ray sources, with the photoelectrons being collected along the sample's surface normal vector. The

as-collected data were analyzed, fitted, and interpreted using a commercial CasaXPS software package. The positions of the peaks were calibrated by using a carbon standard set at 284.8 eV. *Electrochemical characterization:* Prior to depositing the catalysts onto the glassy carbon rotating disk electrode (Pine Research, 5.0 mm), the electrode surface was polished using an aluminum oxide slurry. The catalyst dispersion (2 mg mL^{-1} in ethanol) was drop cast onto the electrode by adding two 5 μL aliquots of the sample dispersion onto the surface; these were allowed to dry in air. Next, a single 5 μL droplet of a 0.025% Nafion solution in ethanol was added to the electrode surface.

For the electrochemical measurements in acid, an aqueous 0.1 M perchloric acid (optima grade, Fisher Scientific) solution was prepared with high-purity water, characterized by a resistivity value of 18.2 MΩ cm. Prior to any measurements, the electrolyte solution was saturated with Ar, that had been bubbled in for about 30 minutes. The electrochemical setup consisted of a platinum wire as the counter electrode and an Ag/AgCl combination (4.0 M KCl with Ag) as the reference electrode. All potentials measured herein were reported with respect to the reversible hydrogen electrode (RHE). Specifically, calibration was performed by bubbling in H_2 gas into the electrolyte and then measuring the open circuit voltage. This value was then added to the measured Ag/AgCl potential in order to convert it to RHE. Cyclic voltammetry curves were acquired, using a scan rate of 20 mV s^{-1} in Ar-saturated 0.1 M perchloric acid.

The oxidation reactions involving methanol, ethanol, and formic acid were performed using a solution incorporating either 0.5 M methanol (optima grade, Fisher Scientific), ethanol (99.9%, Supelco), or formic acid (98+%, Acros Organics), respectively, within a 0.1 M $HClO_4$ solution. Linear sweep voltammetry (LSV) data for the various oxidation reactions were obtained using a scan rate of 20 mV s^{-1}. All of the electrochemical data were normalized to the

Pt's electrochemically active surface area (ECSA), the magnitude of which was derived from the integrated hydrogen adsorption (H_{ads}) area determined from the CV analysis in conjunction with the conversion factor of 210 μC cm^{-2}. The activities of our perovskite-supported catalysts were compared with that of reference commercial carbon-supported samples (TKK TEC10E50E).

For the CO stripping measurements, the same electrochemical setup was employed, with the working electrode prepared in the same analogous manner. First, the working electrode coated with the catalyst was submerged into a 0.1 M $HClO_4$ solution, while CO gas was bubbled in through solution for 15 minutes; in fact, the electrode was kept at a constant voltage of 0.23 V vs. RHE, where no CO oxidation occurred at the surface.[26] The electrode was subsequently removed from the electrolyte, which was then purged with Ar gas for 15 min to remove CO. The electrode was later re-submerged in an Ar-saturated solution, and the CV curves were obtained between 0 and 1 V vs. RHE using a scan rate of 20 mV s^{-1}.

OER and ORR measurements: These electrochemical measurements were performed using a three-electrode setup with a Hg/HgO electrode used as the reference electrode, Pt wire utilized as the counter electrode, and a glassy carbon rotating disk electrode (surface area of 0.196 cm^2) employed as the working electrode. The catalyst inks were prepared by dispersing 4 mg of catalyst and 40 μL of Nafion solution (5 wt%, Sigma Aldrich) in 1 mL of a water-isopropanol solution (3:1 volume ratio), which was sonicated for 30 min. Next, 5 μL of the catalyst ink were deposited onto the surface of the glassy carbon electrode and allowed to dry in air, yielding an approximate mass loading of 20 μg of catalyst. Electrode calibration was performed in a similar manner, as has been already described for the Ag/AgCl electrode used in the SOM oxidation experiments. For OER, LSVs were acquired within an Ar-saturated 0.1 M KOH solution, prepared from KOH pellets (99.98%, Alfa Aesar), at a scan rate of 10 mV s^{-1} between 1.0 and

1.9 V vs. RHE and with a rotation rate of 1600 rpm. The associated chronoamperometry (CA) measurements were collected at an overpotential value of 500 mV (1.73 V). Commercial IrO_2 (99.9%, Aldrich) was used as a control.

For ORR, CVs were obtained within an O_2-saturated 0.1 M KOH solution at a scan rate of 10 mV s^{-1} between 0.05 and 1.1 V vs. RHE using different rotation rates of 400, 900, 1600, and 2500 rpm, respectively. Prior to taking the OER and ORR measurements, an *iR*-correction was obtained by measuring the ohmic drop at 85% compensation.

From the ORR measurements, the electron transfer number (n) could be determined using the Koutecky-Levich equation

$$\frac{1}{J} = \frac{1}{J_K} + \frac{1}{J_L} = \frac{1}{J_k} + \frac{1}{0.62nFD^{\frac{2}{3}}\nu^{-\frac{1}{6}}C\omega^{\frac{1}{2}}}$$

wherein J, J_K, and J_L are the measured current density, kinetic current density, and diffusion limited current density, respectively, F is the Faraday constant (96500 C mol^{-1}), D is the oxygen diffusion coefficient in 0.1 M KOH (1.73×10^{-5} cm^2 s^{-1}), ν is the kinematic viscosity of the 0.1 M KOH solution (0.01 cm^2 s^{-1}), C is the bulk concentration of O_2 in 0.1 M KOH (1.14×10^{-6} mol cm^{-3}, and ω is the angular rotation rate.

Results and Discussion

The double perovskite nanorods reported herein were generated by modifying a previously reported protocol.[27, 28] In particular, the synthesis process consists of two steps, wherein (i) an intermediate species, consisting of a metal hydroxide composite (Figure S1), is initially generated by a hydrothermal reaction and is subsequently (ii) converted to the desired crystalline perovskite structure by annealing at 1000°C. In terms of original contributions towards understanding this protocol, our work herein has demonstrated that the actual pH of the

reaction solution, prior to the hydrothermal reaction, was the most important factor for enabling the formation of the desired nanorods. In fact, varying pH could be used as a reliable means of controlling their size. Based on the conclusions of a series of experiments, we optimized pH values of 12.3 and 13.4 for the dependable synthesis of YCMO and YNMO, respectively.

The XRD patterns of the as-prepared perovskites are shown in Figure 1A. These data are consistent with the formation of not only reasonably pristine YNMO (characterized by some minor NiO impurities) but also pure YCMO. In addition, SEM images of both perovskites (Figure 1B, C) indicate the presence of nanorods, characterized by average diameters of 324 ± 58 and 353 ± 46 nm for YNMO and YCMO, respectively, along with apparent lengths in the microns. Moreover, EDS measurements (Figure 2) indicated that all of the individual elements are evenly and uniformly distributed throughout the isolated nanorods, while maintaining overall chemical compositions which are close to the expected stoichiometries, as shown in Table S1. The individual effects of the various reaction parameters tested are highlighted below.

In an initial series of experiments, we probed the effect of **annealing temperature** on the formation of YCMO by adjusting this temperature reading from 600 to 1000 °C, followed by annealing for 1 h at each of these individual temperatures. XRD patterns of the variously annealed samples (Figure S2A) indicate that at 600, 700, and 800°C, the product mostly consisted of Y_2O_3 and Mn-doped Co_3O_4. The perovskite structure began to form at 900°C and was essentially only fully generated as the main product (albeit with some unwanted impurities) at 1000°C. In addition, SEM images (Figure S2B-G) of the intermediate before annealing and the annealed products themselves indicate that the annealing process does not have a significant impact on the resulting morphology observed, because all of the isolated samples, regardless of annealing temperature, apparently consisted of 1D nanostructures, characterized by average

diameters of ~150-200 nm. Therefore, based on these collective data, 1000°C was determined to be the optimal annealing temperature for creating the desired perovskite structure.

In systematic attempts to remove the impurities noted above, we discovered that the **pH** of the reaction solution, prior to the hydrothermal reaction step, was the key determining factor in terms of not only attaining the desired composition but also reliably altering the size of the resulting nanorods. For example, with YNMO, at a pH below 12.0, the structure consisted mostly of Y_2O_3; the desired YNMO composition became more favorable at a pH value of 12.0 (Figure S3A). Above pH readings of 12.0, varying the pH further had little effect upon the resulting composition, although samples were found to have incorporated minor amounts of Y_2O_3 and NiO impurities.

Moreover, varying the pH led to a significant impact on the morphology of YNMO, as shown in Figure S3B-L, wherein irregularly shaped nanoparticles and larger particles tended to form below a pH of 12.0, whereas nanorods were predominantly generated at and above pH readings of 12.0. Between pH 12.0 and 13.0, nanorods were characterized by average diameters of about 150-200 nm, such that altering the pH value within this range had limited consequences for the observed size. By contrast, increasing the pH still further to 13.3 and 13.8 led to a growth in the observed diameters of the nanorods to 251 ± 46 nm and 533 ± 140 nm, respectively.

A similar type of pH dependent structure and composition was also noted for YCMO. Specifically, the desired anisotropic morphology did not appear until a pH of 12.0 (Figure S4), albeit with some minor Y_2O_3 impurities. By analogy with our prior analysis with YNMO, as the pH was increased, the measured average diameter also increased, such that samples generated at a pH of 12.0, 12.5, and 13.3 exhibited average width values of 178 ± 33, 333 ± 71, and 697 ± 193 nm, respectively (Figure S4B-F). Therefore, for both YNMO and YCMO samples, we found

that carefully controlling the pH can be used as a viable means for tuning the observed diameters of the as-produced perovskite nanorods.

Upon optimizing pH, the **molar ratio of the precursors** was adjusted, specifically by decreasing the Y/Mn ratio, because both YCMO and YNMO incorporated undesirable impurities. For YNMO, as the Y/Mn ratio was decreased from 2 to 1.6, the amount of Y_2O_3 impurities, apparent from the XRD patterns, was significantly diminished coupled with a smaller reduction in residual NiO (Figure S5A). Further decreasing the Y/Mn ratio to 1.5 had little effect upon the composition. Continuing to lower the molar ratio still more down to 1.4 and 1.2 actually led not only to a rise in the amount of Y_2O_3 impurity observed but also to the emergence of a new, unidentified peak situated at 31.1°. It is worth noting that SEM images (Figure S5B-F) of the samples generated at different Y/Mn ratios appeared to maintain similar morphologies.

A similar trend in behavior was also observed for YCMO, wherein a decrease in the Y/Mn molar ratio in general tended to lessen the amount of Y_2O_3 impurity created, as suggested by the XRD patterns shown in Figure S6A. In fact, when a Y/Mn ratio of 1.9 was utilized, we ended up achieving our compositional goal of isolating a completely pure YCMO sample. However, when the Y/Mn ratio was further reduced, peaks corresponding to Co_3O_4 impurities appeared. Again, we found that similar to YNMO, altering the magnitude of the Y/Mn molar ratio seemed to have little to no apparent effect upon the anisotropic morphology of YCMO, as indicated by Figures S6B-D.

Finally, we investigated the effect of changing the **annealing time** on the quality of YNMO by annealing YNMO samples, synthesized using a pH of 12.8, for varying periods of 1, 2, and 4 h, respectively, at 1000°C. XRD patterns of the resulting products, shown in Figure S7A, indicate that the quantity of Y_2O_3 impurities slightly decreased, whereas there was little to

no effect on the amount of NiO impurities generated. Furthermore, the SEM images displayed in Figure S7B-D indicate that increasing annealing time had little to no impact on the resulting morphology. While increasing the annealing time generally reduces the Y_2O_3 impurities while maintaining the desired morphology, it would likely require a significant annealing time period to make an appreciable difference in the measured purity of the isolated sample. Hence, 4 h was chosen as the ideal annealing time.

It is apparent from these experiments that the pH is the most important parameter in obtaining both the desired composition and morphology. This is a plausible assertion, because the formation of the hydroxide intermediates is a crucial step, since all of the metal hydroxides end up precipitating to generate the desired perovskite metal oxides. In effect, a pH of ~12 is needed to precipitate all of the metal hydroxides, because running the reaction at a pH below that value yielded a final product consisting mostly of Y_2O_3, a finding indicative of the fact that $Y(OH)_3$ likely forms at a much higher rate than that of all other potential transition metal hydroxide species. Moreover, this difference in the formation rates of the various metal hydroxides may explain the need to use sub-stoichiometric amounts of the Y precursor to obtain a pure product without any Y_2O_3 impurities. Our overall results suggest that a high enough annealing temperature is also a necessary requirement for successful perovskite fabrication, with increasing temperatures and reaction times leading to the production of purer products.

To summarize, based on an exercise in systematic parameter optimization, we found that we could reliably and routinely generate pure and homogeneous samples, characterized by similar dimensions. Specifically, the optimal hydrothermal synthesis conditions for producing YCMO consisted of using a Y: Mn: Co precursor ratio of 1.9: 1: 1 and a pH of 12.3 followed by annealed at 1000°C for an interval of 4 h, whereas for fabricating YNMO, the relevant reaction

conditions were associated with a Y: Mn: Ni precursor ratio of 1.6: 1: 1 and a pH of 13.4, coupled with annealing at 1000°C for a period of 12 h.

Characterization of Electrocatalysts

Pt nanoparticles were deposited onto the surfaces of our as-prepared perovskite nanorods, so as to investigate their performance as a catalyst support for the electrooxidation of SOMs. Specifically, $NaBH_4$ was utilized as a reducing agent to form the desired Pt nanoparticles in the presence of the perovskite supports. To probe the morphology of the perovskite supports and Pt nanoparticles, HRTEM images were acquired of as prepared perovskites and the corresponding series of perovskite-supported Pt nanoparticles (Figure 3). HRTEM images of both YCMO and YNMO were characterized by measured *d*-spacings of 0.27 nm, which correspond with the anticipated (111) planes of the perovskite oxides. The associated TEM images of YCMO/Pt and YNMO/Pt are indicative of the formation of Pt nanoparticles with average measured sizes of 4.5 ± 1.5 nm, immobilized onto the outer surfaces of the perovskite nanorods. Complementary HRTEM images of these Pt nanoparticles yielded measured *d*-spacings of 0.23 nm, that could be ascribed to the (111) planes of Pt, as expected.

XPS was used to not only characterize the chemical states of the perovskite oxides but also probe the electronic interaction between the Pt nanoparticles and support materials. The survey spectra for the various samples are shown in Figure S8 and indicate the presence of all of the expected elements with no noticeable impurities. The spectra within the Y 3*d* region (Figure 4A) for all samples incorporate peaks located at ~157 eV and 159 eV, which can be assigned to the $3d_{5/2}$ and $3d_{3/2}$ peaks for yttrium oxide, respectively.[29-31] Moreover, YCMO/Pt and YNMO/Pt both possessed additional signals located at ~158.2 and 160.2 eV, which could be attributed to

the $3d_{5/2}$ and $3d_{3/2}$ peaks for $Y_2(CO_3)_3$.[32] In addition, YCMO/Pt maintains peaks, situated at 155.6 and 157.6 eV, which can be ascribed to the $3d_{5/2}$ and $3d_{3/2}$ peaks for Y^0.[33]

The spectrum for the Co 2*p* region (Figure 4B) for YCMO highlights the $2p_{3/2}$ peak located at 780.5 eV, which can be designated as a Co^{2+} species, an assertion which is further confirmed by the presence of a satellite feature present at 786.7 eV.[34, 35] For YNMO, the Ni $2p_{3/2}$ peak is positioned at 855.4 eV and likely corresponds to Ni^{2+}, as shown in Figure 4C.[36] For both YCMO/Pt and YNMO/Pt, the positions of these $2p_{3/2}$ peaks can be found at the slightly lower binding energies of 780 and 855.1 eV, respectively, denoting values suggestive of a small decrease in the oxidation states of both Co and Ni upon the addition of the Pt nanoparticles.

In Figure 4D, the Mn $2p_{3/2}$ and $2p_{1/2}$ peaks for YCMO are positioned at 642.5 and 653.9 eV, respectively, which are consistent not only with the presence of Mn^{4+} but also with the coexistence of 2^+ oxidation states that have been previously observed for Co.[37] Analogous YNMO samples exhibit comparable peaks, corresponding to Mn^{4+} species, which are similar in position, in addition to extra peaks located at 641.7 and 652.9 eV, that can be ascribed to the presence of Mn^{3+};[38-40] this set of results implies the presence of mixed oxidation states for both Mn and Ni. Specifically, the pristine YNMO sample consists of a combination of approximately 75% Mn^{4+}/Ni^{2+} and 25% Mn^{3+}/Ni^{3+} species.

The oxidation state of Mn within YCMO changes upon the addition of Pt nanoparticles, wherein YCMO/Pt displays peaks at 642.2 and 640.8 eV, which can be attributed to the $2p_{3/2}$ peaks corresponding to Mn^{4+} and Mn^{3+}, respectively. In addition, the YNMO/Pt samples maintains peaks at similar locations to what had been observed for YCMO/Pt and YNMO, indicating the likelihood of a mixed oxidation state by analogy to what had been observed with YNMO. Overall, these results appear to indicate that YCMO, YCMO/Pt, YNMO, and YNMO/Pt

incorporate 100, 73, 75, and 74% Mn^{4+} species, respectively. That is, judging by the variability in the Mn^{4+} content, YCMO is more substantially impacted by decoration with Pt nanoparticles as compared with YNMO, indicative of a greater amount of catalyst-support interactions.

The O 1*s* bands (Figure 4E) for each sample could be deconvoluted into a set of four peaks. Prior literature suggests that the associated species can be identified as (i) adsorbed water at ~533.5 eV, (ii) adsorbed OH species at ~532.5 eV, and adsorbed oxygen species, comprised of not only (iii) oxygen vacancies (O_V) located at ~531.3 eV but also (iv) lattice oxygen (O_L) sites situated at ~529.5 eV.[41] In addition, the YCMO/Pt sample exhibited an additional lattice oxygen peak present at 527.9 eV. The O_V/O_L ratios for each sample were calculated in order to analyze the relative abundance of oxygen vacancies present among the various samples. In particular, the O_V/O_L ratios for YCMO and YNMO were determined to be 0.49 and 0.39, respectively, indicating that YCMO possesses a higher amount of oxygen vacancies. By contrast, the O_V/O_L ratios for YCMO/Pt and YNMO/Pt were computed to be almost equivalent in magnitude with values of 0.83 and 0.80, respectively. The latter results imply that any observed differences in the electrocatalytic activity likely will not stem from the relative presence (or absence) of oxygen vacancies alone. What is certain is that this noticeable increase in oxygen vacancy content upon Pt incorporation correlates with the corresponding apparent decrease (albeit small) in the oxidation states of Mn, Co, and Ni, respectively, upon the addition of Pt.

In order to further probe the extent of favorable synergistic metal-support interactions, XPS analysis was performed on the Pt 4*f* bands for YCMO/Pt and YNMO/Pt (Figure 4F). Both samples exhibited two sets of peaks which correspond with Pt^0 and Pt^{2+}, respectively, with Pt^0 assigned as the majority oxidation state of Pt within both samples. Moreover, the Pt^0 $4f_{7/2}$ peaks for YCMO/Pt and YNMO/Pt are situated at 70.4 and 71.0 eV, respectively, which are lower than

that of the bulk Pt signal (71.2 eV).[42] These results imply that the comparatively lower peak position for the YCMO substrate signal can be ascribed in part to its stronger interaction with the Pt catalyst as compared with YNMO.[43, 44]

Electrochemical Activity

CV curves of not only the perovskite/Pt catalyst but also a Pt/C standard used as a control were obtained in an Ar-saturated solution of 0.1 M $HClO_4$, at a scan rate of 20 mV s^{-1}, as shown in Figure 5A. The electrocatalysts all exhibited a hydrogen adsorption region between 0 and 0.4 V in addition to a Pt oxide region between 0.6 and 1.0 V, denoting features which are expected for nanostructured Pt.[45] By comparison with the Pt/C standard, the perovskite-supported catalysts experience a suppression of both regions, which may be a result of a lower Pt loading onto the perovskites (20 wt%) versus that of the standard itself (~50 wt%). This observation is further reinforced by the lower ECSAs noted for the perovskite/Pt catalysts (0.4 cm^2) as compared with that of the Pt/C standard (7.3 cm^2), thereby implying that the perovskite/Pt catalysts incorporate a much lower amount of available Pt and, not surprisingly, give rise to a suppression in the peaks, related to reactions occurring at the Pt sites. However, the position of the oxide reduction peak did not alter very much at all when we compared the activity of the Pt/C standard versus that of the perovskite supports, a finding suggestive of the fact that the perovskites do not appreciably influence the strength of oxygen absorption.

SOM electrooxidation results. The activity towards MOR for each catalyst was measured by taking linear sweep voltammetry (LSV) curves within an Ar-saturated 0.1 M $HClO_4$ solution, containing 0.5 M methanol, using a scan rate of 20 mV s^{-1}. The results were normalized to the Pt's ECSA, as determined by the integration of the hydrogen adsorption region for each individual catalyst, and our data are provided in terms of specific activity. To highlight the

effects of the perovskite supports upon the observed catalytic activity, the results for Pt/C, YCMO/Pt, and YNMO/Pt are compared in Figure 5B and C. It is clear that the perovskite catalysts consistently outperform the Pt/C standard, indicating that the metal oxides represent a superior support material as compared with conventional carbon itself. Specifically, at a reaction potential of 0.8 V, YCMO/Pt exhibits a specific activity, which is 1.3 and 2.1 times higher than that of YNMO/Pt and Pt/C, respectively.

In principle, the electrooxidation of methanol can proceed through two possible pathways: (i) a direct pathway, wherein adsorbed methanol can be converted to either formaldehyde or formic acid which is then subsequently transformed to CO_2, and (ii) an indirect pathway, wherein the adsorbed organic species can be initially converted to adsorbed CO which is then further oxidized to CO_2.[46] In order to evaluate which specific pathway the catalysts undergo during the MOR process, we performed formic acid oxidation reaction (FAOR) measurements, which are often used to determine if methanol is preferentially oxidized via either the direct or indirect mechanism.[47, 48]

Catalysts which pursue the indirect pathway in MOR will also tend to favor the creation of CO within FAOR. We note that the production of CO (and its subsequent oxidation to CO_2) requires a higher potential and yields a distinctive oxidation peak present at ~0.9 V in the forward scan of FAOR. By contrast, catalysts which follow the direct pathway in MOR oxidize formic acid without necessarily forming CO intermediates in a process, which requires lower potentials and generates an oxidation peak located at ~0.6 V, when proceeding with FAOR. Hence, with respect to data acquired from the actual experiments, LSV curves were acquired in Ar-saturated 0.1 M perchloric acid containing 0.5 M formic acid, as shown in Figure S9.

Whereas Pt/C, YCMO/Pt, and YNMO/Pt catalysts all exhibited distinctive oxidation

waves at about 0.6 and 0.9 V, it is worth highlighting that all of these catalysts also gave rise to appreciably higher current densities observed at 0.9 V, thereby suggesting that the indirect pathway for both FAOR and MOR was preferred. Since the indirect mechanism involves the intermediate formation of CO, we can deduce that the perovskite-supported catalysts display superior MOR activity as compared with Pt/C, due to the possibility of a bifunctional mechanism with these metal oxides, wherein the perovskite oxides facilitate the oxidation of CO.

To confirm this assertion, we have performed CO stripping measurements on the different catalysts, as shown in Figure S10. The Pt/C, YCMO/Pt, and YNMO/Pt samples evince distinctive CO oxidation peaks positioned at ~0.85, 0.85, and 0.88 V, respectively. Moreover, these peaks possess onset potentials located at ~0.80, 0.81, and 0.75 V, associated with Pt/C, YNMO/Pt, and YCMO/Pt, respectively. As such, the lowest onset potential measured for the YCMO/Pt sample (i) confirms that CO poisoning species likely can be more easily removed as compared with either Pt/C or YNMO/Pt; (ii) is consistent with a reduced binding strength for CO adsorption; and (iii) is typically associated with a decrease in the position of the Pt *d*-band center.

The activity of each catalyst for EOR was measured by taking LSV curves within an Ar-saturated 0.1 M perchloric acid solution, containing 0.5 M ethanol. Similar to the results for MOR, the EOR data are displayed in terms of the specific activity, as shown in Figure 5D. By analogy with our findings for MOR, it is apparent that the YCMO/Pt catalyst reliably outperforms both the Pt/C and YNMO/Pt catalysts through the majority of the potential window, thereby suggesting that the cobalt-based double perovskite denotes a superior catalyst. Specifically, the perovskite-supported catalysts exhibit two distinctive peaks situated at about 0.87 and 1.22 V, whereas the Pt/C standard gives rise to only one peak located at 1.08 V. Generally, there are two peaks observed in the oxidation of ethanol, wherein the peak situated at

a lower voltage can be attributed to the dehydrogenation of ethanol and is typically used to evaluate the performance of a catalyst. The higher voltage peak can be ascribed to the oxidation process associated with adsorbed oxygen species.[49, 50] As such, the perovskite- supported catalysts yielded a significant improvement in activity, as indicated by the negative shift of about 0.2 V of the ethanol dehydrogenation peak. Moreover, at a reaction potential of 0.8 V, YCMO/Pt achieved a current density value which is 2.3 times higher than that of both Pt/C and YNMO/Pt.

To summarize, the superior activity of YCMO/Pt for both EOR and MOR can largely be attributed to strong, synergistic metal-support interactions, indicated by the decrease in binding energy observed in the Pt 4*f* band. Specifically, the activity for the electrooxidation of SOMs can typically be explained by differences in the position of the *d*-band center of Pt, wherein a lower *d*-band center is usually correlated with a weaker binding energy of adsorbates,[51, 52] in this case CO, an observation which would explain measured improvements in catalytic performance.

XPS is a commonly employed technique to probe changes in the *d*-band center, because shifts in the XPS bands are often correlated with corresponding changes in the position of the *d*-band center. However, there are discrepancies with how shifts in the binding energies precisely relate to the *d*-band centers with some reports suggesting that a negative shift in the binding energy indicates a downshift in the Pt *d*-band center,[53-55] whereas other studies come to exactly the opposite conclusion.[56-58] Therefore, it has been proposed that shifts in the XPS bands can be affected by several factors and that therefore, both trends are possible.[59]

Herein, we observed a downshift in the binding energies for the Pt 4*f* bands for YCMO/Pt as compared with YNMO/Pt, both of which in turn were downshifted as compared to what has been typically expected for bulk Pt^0 itself. These data would appear to indicate stronger metal-support interactions between Pt and the underlying perovskites as compared with between Pt and

carbon. Moreover, our results further suggest that there is a more pronounced decrease in the Pt -*d*-band center in YCMO/Pt as compared with the other catalysts analyzed, an assertion corroborated not only by the accompanying CO stripping results but also by the lowest onset potentials measured in this study, which were associated with YCMO/Pt.

OER Results. We evaluated the electrocatalytic activity towards OER not only for the bare perovskites but also for IrO_2 as a control sample. Figure 6A displays the iR-corrected LSV curves for YCMO, YNMO, and IrO_2 within an Ar-saturated 0.1 M KOH solution. The overpotentials required to achieve a current density of 10 mA/cm^2 were determined to be 520 and 590 mV for IrO_2 and YCMO, respectively, while YNMO did not achieve 10 mA/cm^2 within the measured potential range. It should be noted that the activity for the IrO_2 control used herein is lower than what would have been expected for IrO_2 nanoparticles and accordingly, was attributed to the larger size of the commercial IrO_2 used herein, as shown in Figure S11. The OER performance of YCMO was compared with that of other perovskite oxides, that have been recently reported; results from the cumulative studies are summarized in Table S2.

To provide a better understanding of the OER mechanism on the perovskite catalysts, the Tafel slopes were measured and plotted (Figure 6B). Specifically, the Tafel slopes for YCMO and YNMO were calculated to be 73 and 157 mV dec^{-1}, respectively, whereas IrO_2 yielded two distinctive slopes of 63 and 127 mV dec^{-1}. These results collectively indicate that YCMO possesses much faster reaction kinetics for OER as compared with YNMO, and even maintains improved kinetics as compared with IrO_2 at higher potentials. Furthermore, the Tafel slope for YCMO is comparable to that of many other perovskites, reported in the literature (Table S2).[60, 61]

A set of CA measurements was acquired at an overpotential of 500 mV to evaluate the stability of the catalysts, and these data are shown in Figure 6C. Interestingly, the current for

YCMO initially rapidly decreases, but then increases steadily where it peaks after about 20 min after which it slowly decreases in activity up to 60 min, while maintaining a higher activity as compared with both IrO_2 and YNMO. In order to understand this unusual behavior during the CA measurements, HRTEM images were acquired of YCMO samples after exposure to an overpotential of 500 mV for 5, 20, and 60 min (Figure 6D-F).

As compared with the pristine, unreacted sample, which maintains a clean surface, the samples, which had been exposed to a constant voltage, exhibited amorphous features. Indeed, the thickness of the isolated amorphous layer increased in size with measured thicknesses of 1.6 ± 0.1, 2.3 ± 0.2, and 3.1 ± 0.1 nm after 5, 20, and 60 min, respectively. A similar scenario played out with La_2NiMnO_6 nanoparticles, wherein an 'active layer' was formed after cycling during OER.[9] As such, the formation of this layer can be used to explain not only the observed increase in performance but also the improved stability of YCMO, as compared with IrO_2, which is known to experience deleterious degradation effects during cycling.[62]

The dramatic difference in the OER activity between YCMO and YNMO can likely be attributed to differences in the electronic structure between these two double perovskites, since it has been previously reported that that the optimal average e_g filling for OER catalysts is typically set to be around one.[63] As alluded to in our XPS discussion, Co and Mn can exist in the 2^+ and 4^+ oxidation states, respectively, the former of which maintains a high-spin state.[64] As such, Mn^{4+} possesses an electronic configuration of $t_{2g}^3e_g^0$, whereas the high-spin Co^{2+} is characterized by an electronic configuration of $t_{2g}^5e_g^2$, thereby giving rise to an average e_g occupation of one.

In the context of La_2CoMnO_6, it was reported that this type of configuration yielded the highest activities, whereas samples consisting mostly of Mn^{3+} and Co^{3+} displayed lower activities.[10] In fact, the higher activity of the Mn^{4+}–O–Co^{2+} configuration can likely be attributed

to vibronic superexchange, wherein the Co^{2+} e_g electrons can be transferred to the empty Mn^{4+} e_g orbitals,[64, 65] leading to Jahn-Teller distortion, which can cause the formation of the catalytically active species observed at the outer surface of YCMO during OER.[9] Whereas the Ni^{2+} and Mn^{4+} species within YNMO possess the same e_g orbital occupations as Co^{2+} and Mn^{4+} within YCMO, by contrast, the Ni^{2+} electronic configuration of $t_{2g}^6e_g^2$ inhibits Jahn-Teller distortion at the Ni^{2+} site and as such, there is no vibronic superexchange between the Ni^{2+} and Mn^{4+} ions.[66]

Moreover, it should be noted that within YNMO, the combinations of Ni^{2+}-Mn^{4+} and Ni^{3+}-Mn^{4+} both exhibit an average e_g orbital occupation of one, which would suggest that either configuration should give rise to favorable OER activity. However, this is not necessarily the case, because occupations of e_g^2 or e_g^0 can render the metal-oxygen bonds as either too weak or too strong, respectively.[63, 67] That is, YNMO consists of a mixture of oxidation states, wherein Mn^{4+} and Ni^{2+} species make up 75%, while the remainder consists of Mn^{3+} and Ni^{3+}. As such, the YNMO chemical composition is actually unfavorable for OER activity, due to an average e_g occupation value which deviates substantially from the ideal of unity. In this vein, Jiang *et al.* have proposed an amendment to the e_g-filling rule by describing the average deviation from unity e_g occupation (D),[10] which can be calculated using Equation 1, provided as follows:

$$D = \Sigma_{mn} \mid e_{g(mn)} - 1 \mid \times P_{mn} \qquad \text{(Equation 1)}$$

wherein m represents the transition metal ion, n is the spin state, $e_{g(mn)}$ is the e_g orbital occupation number of the mth transition metal ion with nth spin state, and P_{mn} is the ratio of the transition metal ions. For YNMO, the P_{mn} values, obtained from the XPS measurements, were computed to be ~37.5, 37.5, 12.5, and 12.5 for Mn^{4+}, Ni^{2+}, Mn^{3+}, and Ni^{3+} species, respectively. Therefore, by calculating for D, it was determined that YNMO gave rise to an average deviation of 0.75, which can explain its low OER activity to a large extent. That is, the significant

improvement in OER activity observed in YCMO as compared with YNMO can be explained by a combination of Jahn-Teller distortions and vibronic superexchange effects.

ORR Results. In an effort to demonstrate the further versatility and potential of Y-based double perovskites potential as bifunctional catalysts, we have also performed ORR measurements, as shown in Figure S12. YCMO and YNMO samples achieved an activity of -1 mA cm^{-2}, which was attained at potentials of 0.632 and 0.627 V, respectively. It is interesting that there is little difference in the ORR activity for YNMO and YCMO, which suggests that the composition itself does not have as large of an effect as compared with that for OER. From our ORR data, YCMO was found to exhibit a bifunctional index (BI) of 1.19 V, which is defined as the difference in potentials between the ORR potential at -1 mA cm^{-2} and the OER overpotential. It should be noted that YNMO cannot function as a bifunctional catalyst, since it does not achieve a current density threshold of 10 mA cm^{-2} for OER. Moreover, Koutecky-Levich analysis was used to determine the electron transfer number of each catalyst; this was determined to be ~2.8, 2.7, and 2.7 for YCMO, YNMO, and IrO_2, respectively, which suggests that the catalysts undergo a quasi-two-electron process. These results indicate that YCMO can act as a bifunctional catalyst towards both OER and ORR. Table S3 provides a comparison between recently reported perovskite oxide bifunctional catalysts from the literature.

Conclusions

YCMO and YNMO nanorods with average diameters of about 300 nm were generated by a two-step procedure, wherein (i) a metal hydroxide composite intermediate is formed by a hydrothermal procedure followed by (ii) annealing at high temperature to yield the desired double perovskites. The optimal conditions for the synthesis of both double perovskites were

determined by varying different synthetic reaction parameters, such as the pH, annealing temperature, annealing time, and the precursor ratios. Based on these collective runs, it was concluded that the pH yielded the largest effect on the resulting morphology of the nanorods; in fact, varying the pH could be effectively used to tune measured diameters. It is worth highlighting that replicate experiments run several times at a number of specific, individual pH values could be reliably reproduced with little if any apparent change in either the observed morphology or the size of the ensuing product. In addition, it was discovered that precisely altering other variables, including not only the annealing temperature and time but also the metal precursor ratio, enabled the isolation of compositionally pure perovskite nanorods. Specifically, an annealing temperature of 1000°C was necessary to generate a sample consisting mostly of the expected perovskite structure, whereas increasing the reaction time also decreased the amount of unwanted metal oxide impurities. Tailoring the metal precursor ratio similarly reduced undesirable metal oxide precursors.

The double perovskite nanorods were subsequently utilized as supports for Pt nanoparticles, giving rise to YCMO/Pt and YNMO/Pt catalysts, which were used for the oxidation of methanol and ethanol within acidic media. When used for MOR, the YCMO/Pt catalysts maintained performance metrics, which were 1.3 and 2.1 times higher than what were obtained for YNMO/Pt and Pt/C, respectively. It is believed that MOR on the YCMO/Pt catalysts proceeds by an indirect pathway, involving the formation of an adsorbed CO intermediate, an assertion which is confirmed by FAOR measurements. Furthermore, YCMO/Pt exhibited activities towards EOR, which were 2.3 times higher than that of both Pt/C and YNMO/Pt. In general, the increased performance of YCMO/Pt towards the oxidation of SOMs

can largely be explained by strong and favorable metal-support interactions, an assertion corroborated by a combination of XPS and CO stripping measurements.

When used as catalysts for OER, YCMO exhibited an overpotential of 590 mV, which is slightly higher than that of commercial IrO_2 (520 mV), while YNMO gave rise to very little activity whatsoever. Moreover, YCMO demonstrated superior stability, where after an initial decrease in activity was noted, there was a subsequent rise in activity, which appeared to peak after about 20 min and then slowly decreased, when exposed to an overpotential of 500 mV. By contrast, the analogous YNMO yielded a relatively poor OER activity. We have ascribed the enhancement in both the performance and stability of YCMO as compared with YNMO to differences in the electronic spin configurations of Co versus that of Ni. Specifically, our findings indicate that the OER activity within double perovskites can be controlled by carefully tuning the oxidation states and corresponding electronic configuration of these metal oxides.

In summary, this report highlights the versatile multi-functionality of Y-based double perovskites utilized not only as supports for MOR and EOR but also as catalysts for OER. It was determined that chemical composition plays an important role in the observed activity for all of the various reactions. In particular, the Co-based double perovskite support yielded improved synergistic metal-support interactions as compared with YNMO, indicative of a decrease in the position of the *d*-band center of the overlying Pt. YCMO also evinced superior performance towards OER as compared with YNMO, an observation which can be attributed to differences in electronic configuration wherein the existence of high-spin Co^{2+} species allows for vibronic superexchange with Mn^{4+}, thereby forming a catalytically active layer at the surface. These results collectively indicate that Y-based double perovskites can be considered as both promising

catalysts and support materials. Significantly, we have shown that the identity of the constituent B-site metals (i.e. Co vs. Ni) can significantly impact the observed electrocatalytic metrics.

Acknowledgements

This material is based on work supported by the U.S. National Science Foundation under Grant No. CHE-1807640. Structural characterization experiments (TEM, SEM, and XPS) for this manuscript were performed in part at the Center for Functional Nanomaterials, an Office of Science facility located at Brookhaven National Laboratory, which is supported by the U.S. Department of Energy under Contract No. DE-SC0012704.

Supporting Information

XRD of the intermediate species; characterization data obtained on samples generated by varying reaction parameters; survey XPS spectra of all perovskite catalysts; typical LSV curves collected for FAOR; representative CO stripping curves for SOM oxidation catalysts; SEM images of commercial IrO_2; along with tables summarizing elemental compositions and prior comparative OER/ORR literature data.

References

1. Sun, H.; Song, S.; Xu, X.; Dai, J.; Yu, J.; Zhou, W.; Shao, Z.; Jung, W., Recent Progress on Structurally Ordered Materials for Electrocatalysis. *Adv. Energy Mater.* **2021,** *11* (37), 2101937.
2. Yin, W.-J.; Weng, B.; Ge, J.; Sun, Q.; Li, Z.; Yan, Y., Oxide Perovskites, Double Perovskites and Derivatives for Electrocatalysis, Photocatalysis, and Photovoltaics. *Energy Environ. Sci.* **2019,** *12* (2), 442-462.
3. Kumar, A.; Kumar, A.; Krishnan, V., Perovskite Oxide Based Materials for Energy and Environment-Oriented Photocatalysis. *ACS Catal.* **2020,** *10* (17), 10253-10315.
4. Yu, J.; Ran, R.; Zhong, Y.; Zhou, W.; Ni, M.; Shao, Z., Advances in Porous Perovskites: Synthesis and Electrocatalytic Performance in Fuel Cells and Metal-Air Batteries. *Energy Environ. Mater.* **2020,** *3* (2), 121-145.
5. Zhu, L.; Ran, R.; Tade, M.; Wang, W.; Shao, Z., Perovskite Materials in Energy Storage and Conversion. *Asia-Pac. J. Chem. Eng.* **2016,** *11* (3), 338-369.
6. Xu, X.; Su, C.; Shao, Z., Fundamental Understanding and Application of $Ba_{0.5}Sr_{0.5}Co_{0.8}Fe_{0.2}O_{3-\delta}$ Perovskite in Energy Storage and Conversion: Past, Present, and Future. *Energy & Fuels* **2021,** *35* (17), 13585-13609.
7. Li, L.; Tan, S.; Salvatore, K. L.; Wong, S. S., Nanoscale Perovskites as Catalysts and Supports for Direct Methanol Fuel Cells. *Chem. - Eur. J.* **2019,** *25* (33), 7779-7797.
8. Xu, X.; Zhong, Y.; Shao, Z., Double Perovskites in Catalysis, Electrocatalysis, and Photo(electro)catalysis. *Trends in Chemistry* **2019,** *1* (4), 410-424.
9. Tong, Y.; Wu, J.; Chen, P.; Liu, H.; Chu, W.; Wu, C.; Xie, Y., Vibronic Superexchange in Double Perovskite Electrocatalyst for Efficient Electrocatalytic Oxygen Evolution. *J. Am. Chem. Soc.* **2018,** *140* (36), 11165-11169.
10. Jiang, M.; Li, J.; Zhao, Y.; Pan, L.; Cao, Q.; Wang, D.; Du, Y., Double Perovskites as Model Bifunctional Catalysts toward Rational Design: The Correlation between Electrocatalytic Activity and Complex Spin Configuration. *ACS Appl. Mater. Interfaces* **2018,** *10* (23), 19746-19754.
11. Lee, H.; Gwon, O.; Choi, K.; Zhang, L.; Zhou, J.; Park, J.; Yoo, J.-W.; Wang, J.-Q.; Lee, J. H.; Kim, G., Enhancing Bifunctional Electrocatalytic Activities via Metal d-Band Center Lift Induced by Oxygen Vacancy on the Subsurface of Perovskites. *ACS Catal.* **2020,** *10*, 4664−4670.
12. Gupta, S.; Kellogg, W.; Xu, H.; Liu, X.; Cho, J.; Wu, G., Bifunctional Perovskite Oxide Catalysts for Oxygen Reduction and Evolution in Alkaline Media. *Chem. Asian J.* **2016,** *11*, 10-21.
13. Hong, W. T.; Risch, M.; Stoerzinger, K. A.; Grimaud, A.; Suntivich, J.; Shao-Horn, Y., Toward the Rational Design of Non-Precious Transition Metal Oxides for Oxygen Electrocatalysis. *Energy Environ. Sci.* **2015,** *8*, 1404-1427.
14. Hua, B.; Sun, Y.-F.; Li, M.; Yan, N.; Chen, J.; Zhang, Y.-Q.; Zeng, Y.; Amirkhiz, B. S.; Luo, J.-L., Stabilizing Double Perovskite for Effective Bifunctional Oxygen Electrocatalysis in Alkaline Conditions. *Chem. Mater.* **2017,** *29*, 6228−6237.
15. Xu, X.; Pan, Y.; Zhong, Y.; Shi, C.; Guan, D.; Ge, L.; Hu, Z.; Chin, Y.-Y.; Lin, H.-J.; Chen, C.-T.; Wang, H.; Jiang, S. P.; Shao, Z., New Undisputed Evidence and Strategy for Enhanced Lattice-Oxygen Participation of Perovskite Electrocatalyst through Cation Deficiency Manipulation. *Adv. Sci.* **2022,** *9* (14), 2200530.

16. Sun, J.; Du, L.; Sun, B.; Han, G.; Ma, Y.; Wang, J.; Huo, H.; Du, C.; Yin, G., Bifunctional $LaMn_{0.3}Co_{0.7}O_3$ Perovskite Oxide Catalyst for Oxygen Reduction and Evolution Reactions: The Optimized eg Electronic Structures by Manganese Dopant. *ACS Appl. Mater. Interfaces* **2020,** *12* (22), 24717-24725.
17. Xue, Y.; Xin, H.; Xie, W.; Wu, P.; Li, X., Pt nanoparticles Supported on $YCo_xFe_{1-x}O_3$ Perovskite Oxides: Highly Efficient Catalysts for Liquid-Phase Hydrogenation of Cinnamaldehyde. *Chem. Commun.* **2019,** *55* (23), 3363-3366.
18. Mao, X.; Lin, C.; Graham, G. W.; Gorte, R. J., A Perspective on Thin-Film Perovskites as Supports for Metal Catalysts. *ACS Catal.* **2020,** *10* (15), 8840-8849.
19. Li, J.; Guan, Q.; Wu, H.; Liu, W.; Lin, Y.; Sun, Z.; Ye, X.; Zheng, X.; Pan, H.; Zhu, J.; Chen, S.; Zhang, W.; Wei, S.; Lu, J., Highly Active and Stable Metal Single-Atom Catalysts Achieved by Strong Electronic Metal−Support Interactions. *J. Am. Chem. Soc.* **2019,** *141*, 14515−14519.
20. Ji, Q.; Bi, L.; Zhang, J.; Cao, H.; Zhao, X. S., The Role of Oxygen Vacancies of ABO_3 Perovskite Oxides in the Oxygen Reduction Reaction. *Energy Environ. Sci.* **2020,** *13*, 1408--1428.
21. Zhu, Y.; Liu, X.; Jin, S.; Chen, H.; Lee, W.; Liu, M.; Chen, Y., Anionic Defect Engineering of Transition Metal Oxides for Oxygen Reduction and Evolution Reactions. *J. Mater. Chem. A* **2019,** *7*, 5875–5897.
22. McGuire, S. C.; Koenigsmann, C.; Chou, C. C.; Tong, X.; Wong, S. I. S., Lanthanum-Based Double Perovskite Nanoscale Motifs as Support Media for the Methanol Oxidation Reaction. *Catal. Sci. Technol.* **2022,** *12* (2), 613-629.
23. Xu, X.; Wang, W.; Zhou, W.; Shao, Z., Recent Advances in Novel Nanostructuring Methods of Perovskite Electrocatalysts for Energy-Related Applications. *Small Methods* **2018,** *2* (7), 1800071.
24. Meher, S. K.; Rao, G. R., Morphology-Controlled Promoting Activity of Nanostructured MnO_2 for Methanol and Ethanol Electrooxidation on Pt/C. *J. Phys. Chem. C* **2013,** *117* (10), 4888-4900.
25. Wang, Z.; Li, M.; Liang, C.; Fan, L.; Han, J.; Xiong, Y., Effect of Morphology on the Oxygen Evolution Reaction for $La_{0.8}Sr_{0.2}Co_{0.2}Fe_{0.8}O_{3-\delta}$ Electrochemical Catalyst in Alkaline Media. *RSC Adv.* **2016,** *6* (73), 69251-69256.
26. Nilekar, A. U.; Sasaki, K.; Farberow, C. A.; Adzic, R. R.; Mavrikakis, M., Mixed-Metal Pt Monolayer Electrocatalysts with Improved CO Tolerance. *J. Am. Chem. Soc.* **2011,** *133* (46), 18574-18576.
27. Alam, M.; Karmakar, K.; Pal, M.; Mandal, K., Electrochemical Supercapacitor Based on Double Perovskite Y_2NiMno_6 Nanowires. *RSC Adv.* **2016,** *6* (115), 114722-114726.
28. Alam, M.; Mandal, K.; Khan, G. G., Double Perovskite Y_2NiMnO_6 Nanowires: High Temperature Ferromagnetic–Ferroelectric Multiferroic. *RSC Adv.* **2016,** *6* (67), 62545-62549.
29. Craciun, V.; Howard, J.; Lambers, E. S.; Singh, R. K.; Craciun, D.; Perriere, J., Low-Temperature Growth of Y_2O_3 Thin Films by Ultraviolet-Assisted Pulsed Laser Deposition. *Appl. Phys. A* **1999,** *69* (1), S535-S538.
30. Alam, M.; Mandal, K.; Khan, G. G., Origin and Tuning of Room Temperature Ferromagnetism and Ferroelectricity in Double Perovskite Y_2NiMnO_6 Nanostructured Thin Films. *J. Alloys Compd.* **2020,** *822*, 153540.
31. Cheng, X.; Qi, Z.; Zhang, G.; Zhou, H.; Zhang, W.; Yin, M., Growth and Characterization of Y_2O_3 Thin Films. *Phys. B: Condens. Matter* **2009,** *404* (1), 146-149.

32. Zhang, Y.; Gao, M.; Han, K.; Fang, Z.; Yin, X.; Xu, Z., Synthesis, Characterization and Formation Mechanism of Dumbbell-like $YOHCO_3$ and Rod-like $Y_2(CO_3)_3 \cdot 2.5H_2O$. *J. Alloys Compd.* **2009,** *474* (1), 598-604.
33. Brandiele, R.; Guadagnini, A.; Girardi, L.; Dražić, G.; Dalconi, M. C.; Rizzi, G. A.; Amendola, V.; Durante, C., Climbing the Oxygen Reduction Reaction Volcano Plot with Laser Ablation Synthesis of Pt_xY Nanoalloys. *Catal. Sci. Technol.* **2020,** *10* (14), 4503-4508.
34. Silva, R. X.; Almeida, R. M.; Moreira, R. L.; Paniago, R.; Rezende, M. V. S.; Paschoal, C. W. A., Vibrational Properties and Infrared Dielectric Features of Gd_2CoMnO_6 and Y_2CoMnO_6 Double Perovskites. *Ceram. Int.* **2019,** *45* (4), 4756-4762.
35. Guo, H. Z.; Gupta, A.; Calvarese, T. G.; Subramanian, M. A., Structural and Magnetic Properties of Epitaxial Thin Films of the Ordered Double Perovskite La_2CoMnO_6. *Appl. Phys. Lett.* **2006,** *89* (26), 262503/1-262503/3.
36. Zhang, C.; Zhang, T.; Ge, L.; Wang, S.; Yuan, H.; Feng, S., Hydrothermal Synthesis and Multiferroic Properties of Y_2NiMnO_6. *RSC Adv.* **2014,** *4* (92), 50969-50974.
37. Su, J.; Yang, Z. Z.; Lu, X. M.; Zhang, J. T.; Gu, L.; Lu, C. J.; Li, Q. C.; Liu, J. M.; Zhu, J. S., Magnetism-Driven Ferroelectricity in Double Perovskite Y_2NiMnO_6. *ACS Appl. Mater. Interfaces* **2015,** *7* (24), 13260-13265.
38. Zhao, H.; Sun, L.; Fu, M.; Mao, L.; Zhao, X.; Zhang, X.; Xiao, Y.; Dong, G., Effect of A-Site Substitution on the Simultaneous Catalytic Removal of NO_x and Soot by $LaMnO_3$ Perovskites. *New J. Chem.* **2019,** *43* (29), 11684-11691.
39. Xia, W.; Wu, H.; Xue, P.; Zhu, X., Microstructural, Magnetic, and Optical Properties of Pr-Doped Perovskite Manganite $La_{0.67}Ca_{0.33}MnO_3$ Nanoparticles Synthesized via Sol-Gel Process. *Nanoscale Res. Lett.* **2018,** *13* (1), 1-13.
40. Das, R.; Jaiswal, A.; Poddar, P., Static and Dynamic Magnetic Properties and Interplay of Dy^{3+}, Gd^{3+} and Mn^{3+} Spins in Orthorhombic $DyMnO_3$ and $GdMnO_3$ Nanoparticles. *J. Phys. D: Appl. Phys.* **2013,** *46* (4), 045301/1-045301/7.
41. Luo, Y.; Zheng, Y.; Feng, X.; Lin, D.; Qian, Q.; Wang, X.; Zhang, Y.; Chen, Q.; Zhang, X., Controllable P Doping of the $LaCoO_3$ Catalyst for Efficient Propane Oxidation: Optimized Surface Co Distribution and Enhanced Oxygen Vacancies. *ACS Appl. Mater. Interfaces* **2020,** *12* (21), 23789-23799.
42. Moulder, J. F.; Chastain, J., *Handbook of X-ray Photoelectron Spectroscopy*. Physical Electronics Division, Perkin-Elmer Corporation: 1992.
43. Xiong, L.; Yang, X.; Xu, M.; Xu, Y.; Wu, D., Pt-Ni Alloy Nanoparticles Supported on Multiwalled Carbon Nanotubes for Methanol Oxidation in Alkaline Media. *J. Solid State Electrochem.* **2013,** *17* (3), 805-810.
44. Kim, D. B.; Chun, H.-J.; Lee, Y. K.; Kwon, H.-H.; Lee, H.-I., Preparation of Pt/NiO-C Electrocatalyst and Heat-Treatment Effect on its Electrocatalytic Performance for Methanol Oxidation. *Int. J. Hydrogen Energy* **2010,** *35* (1), 313-320.
45. Garsany, Y.; Baturina, O. A.; Swider-Lyons, K. E.; Kocha, S. S., Experimental Methods for Quantifying the Activity of Platinum Electrocatalysts for the Oxygen Reduction Reaction. *Anal. Chem.* **2010,** *82* (15), 6321-6328.
46. Neurock, M.; Janik, M.; Wieckowski, A., A First Principles Comparison of the Mechanism and Site Requirements for the Electrocatalytic Oxidation of Methanol and Formic Acid Over Pt. *Faraday Discuss.* **2008,** *140* (Electrocatalysis--Theory and Experiment at the Interface), 363-378.

47. Smina, N.; Rosen, A.; Sztaberek, L.; Beatrez, W.; Kingsbury, K.; Troia, R.; Wang, Y.; Zhao, J.; Schrier, J.; Koenigsmann, C., Enhanced Electrocatalytic Oxidation of Small Organic Molecules on Platinum-Gold Nanowires: Influence of the Surface Structure and Pt-Pt/Pt-Au Pair Site Density. *ACS Appl. Mater. Interfaces* **2021,** *13* (50), 59892-59903.
48. Cui, C.-H.; Li, H.-H.; Cong, H.-P.; Yu, S.-H.; Tao, F., Direct Evidence for Active Site-Dependent Formic Acid Electro-Oxidation by Topmost-Surface Atomic Redistribution in a Ternary PtPdCu Electrocatalyst. *Chem. Commun.* **2012,** *48* (99), 12062-12064.
49. Zhao, X.; Zhao, H.; Sun, J.; Li, G.; Liu, R., Blocking the Defect Sites on Ultrathin Pt Nanowires with Rh Atoms to Optimize the Reaction Path toward Alcohol Fuel Oxidation. *Chin. Chem. Lett.* **2020,** *31* (7), 1782-1786.
50. Zhang, Q.; Chen, T.; Jiang, R.; Jiang, F., Comparison of Electrocatalytic Activity of $Pt_{1-x}Pd_x$/C Aatalysts for Ethanol Electro-Oxidation in Acidic and Alkaline Media. *RSC Adv.* **2020,** *10* (17), 10134-10143.
51. Wakisaka, M.; Mitsui, S.; Hirose, Y.; Kawashima, K.; Uchida, H.; Watanabe, M., Electronic Structures of Pt-Co and Pt-Ru Alloys for CO-Tolerant Anode Catalysts in Polymer Electrolyte Fuel Cells Studied by EC-XPS. *J. Phys. Chem. B* **2006,** *110* (46), 23489-23496.
52. Ruban, A.; Hammer, B.; Stoltze, P.; Skriver, H. L.; Norskov, J. K., Surface Electronic Structure and Reactivity of Transition and Noble Metals. *J. Mol. Catal. A: Chem.* **1997,** *115* (3), 421-429.
53. Zheng, J.; Cullen, D. A.; Forest, R. V.; Wittkopf, J. A.; Zhuang, Z.; Sheng, W.; Chen, J. G.; Yan, Y., Platinum-Ruthenium Nanotubes and Platinum-Ruthenium Coated Copper Nanowires As Efficient Catalysts for Electro-Oxidation of Methanol. *ACS Catal.* **2015,** *5* (3), 1468-1474.
54. Wang, L.-L.; Zhang, D.-F.; Guo, L., Phase-Segregated Pt-Ni Chain-Like Nanohybrids with High Electrocatalytic Activity towards Methanol Oxidation Reaction. *Nanoscale* **2014,** *6* (9), 4635-4641.
55. Gu, Z.; Bin, D.; Feng, Y.; Zhang, K.; Wang, J.; Yan, B.; Li, S.; Xiong, Z.; Wang, C.; Shiraishi, Y.; Du, Y., Seed-Mediated Synthesis of Crosslinked Pt-NiO Nanochains for Methanol Oxidation. *Appl. Surf. Sci.* **2017,** *411*, 379-385.
56. Toda, T.; Igarashi, H.; Uchida, H.; Watanabe, M., Enhancement of the Electroreduction of Oxygen on Pt Alloys with Fe, Ni, and Co. *J. Electrochem. Soc.* **1999,** *146* (10), 3750-3756.
57. Li, H.-H.; Zhao, S.; Gong, M.; Cui, C.-H.; He, D.; Liang, H.-W.; Wu, L.; Yu, S.-H., Ultrathin PtPdTe Nanowires as Superior Catalysts for Methanol Electrooxidation. *Angew. Chem., Int. Ed.* **2013,** *52* (29), 7472-7476.
58. Igarashi, H.; Fujino, T.; Zhu, Y.; Uchida, H.; Watanabe, M., CO Tolerance of Pt Alloy Electrocatalysts for Polymer Electrolyte Fuel Cells and the Detoxification Mechanism. *Phys. Chem. Chem. Phys.* **2001,** *3* (3), 306-314.
59. Poh, C. K.; Tian, Z.; Gao, J.; Liu, Z.; Lin, J.; Feng, Y. P.; Su, F., Nanostructured Trimetallic Pt/FeRuC, Pt/NiRuC, and Pt/CoRuC Catalysts for Methanol Electrooxidation. *J. Mater. Chem.* **2012,** *22* (27), 13643-13652.
60. Wang, H.; Zhou, M.; Choudhury, P.; Luo, H., Perovskite Oxides as Bifunctional Oxygen Electrocatalysts for Oxygen Evolution/Reduction Reactions – A Mini Review. *Applied Materials Today* **2019,** *16*, 56-71.
61. Liu, D.; Zhou, P.; Bai, H.; Ai, H.; Du, X.; Chen, M.; Liu, D.; Ip, W. F.; Lo, K. H.; Kwok, C. T.; Chen, S.; Wang, S.; Xing, G.; Wang, X.; Pan, H., Development of Perovskite Oxide-Based Electrocatalysts for Oxygen Evolution Reaction. *Small* **2021,** *17* (43), 2101605.

62. Zagalskaya, A.; Alexandrov, V., Mechanistic Study of IrO2 Dissolution during the Electrocatalytic Oxygen Evolution Reaction. *J. Phys. Chem. Lett.* **2020,** *11* (7), 2695-2700.
63. Suntivich, J.; May, K. J.; Gasteiger, H. A.; Goodenough, J. B.; Shao-Horn, Y., A Perovskite Oxide Optimized for Oxygen Evolution Catalysis from Molecular Orbital Principles. *Science* **2011,** *334* (6061), 1383-1385.
64. Jia, T.; Zeng, Z.; Li, X. G.; Lin, H. Q., The Magnetic Origin of Multiferroic Y_2CoMnO_6. *J. Appl. Phys.* **2015,** *117* (17), 17E119/1-17E119/4.
65. Dass, R. I.; Goodenough, J. B., Multiple Magnetic Phases of $La_2CoMnO_{6-\delta}$ ($0\leq\delta\leq0.05$). *Phys. Rev. B: Condens. Matter Mater. Phys.* **2003,** *67* (1), 014401/1-014401/9.
66. Zhao, S.; Shi, L.; Zhou, S.; Zhao, J.; Yang, H.; Guo, Y., Size-Dependent Magnetic Properties and Raman Spectra of La_2NiMnO_6 Nanoparticles. *J. Appl. Phys.* **2009,** *106* (12), 123901/1-123901/5.
67. Suntivich, J.; Gasteiger, H. A.; Yabuuchi, N.; Nakanishi, H.; Goodenough, J. B.; Shao-Horn, Y., Design Principles for Oxygen-Reduction Activity on Perovskite Oxide Catalysts for Fuel Cells and Metal-Air Batteries. *Nat. Chem.* **2011,** *3* (7), 546-550.

Figures

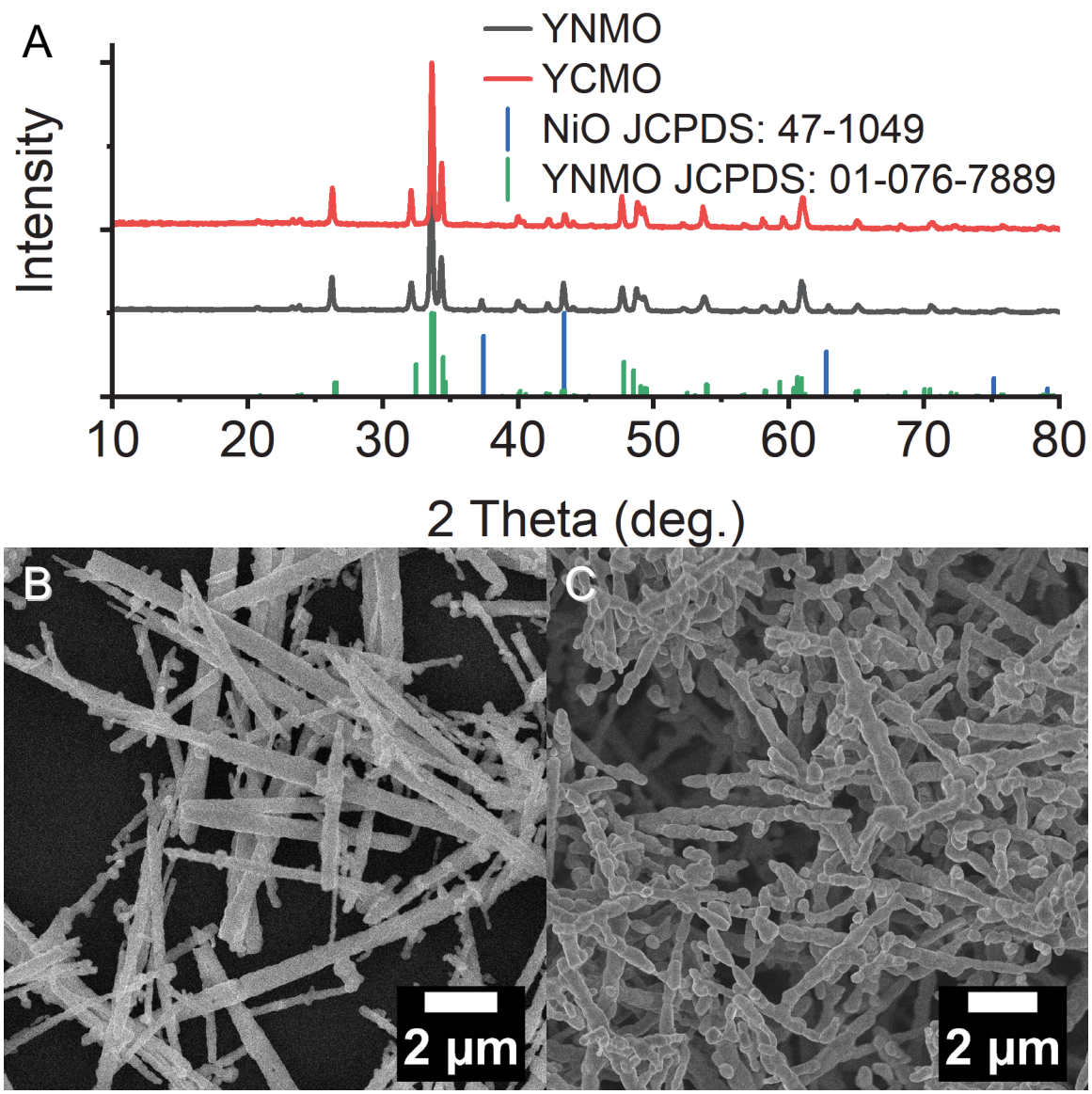

Figure 1. (A) XRD patterns and (B, C) SEM images of (B) YNMO and (C) YCMO nanorods.

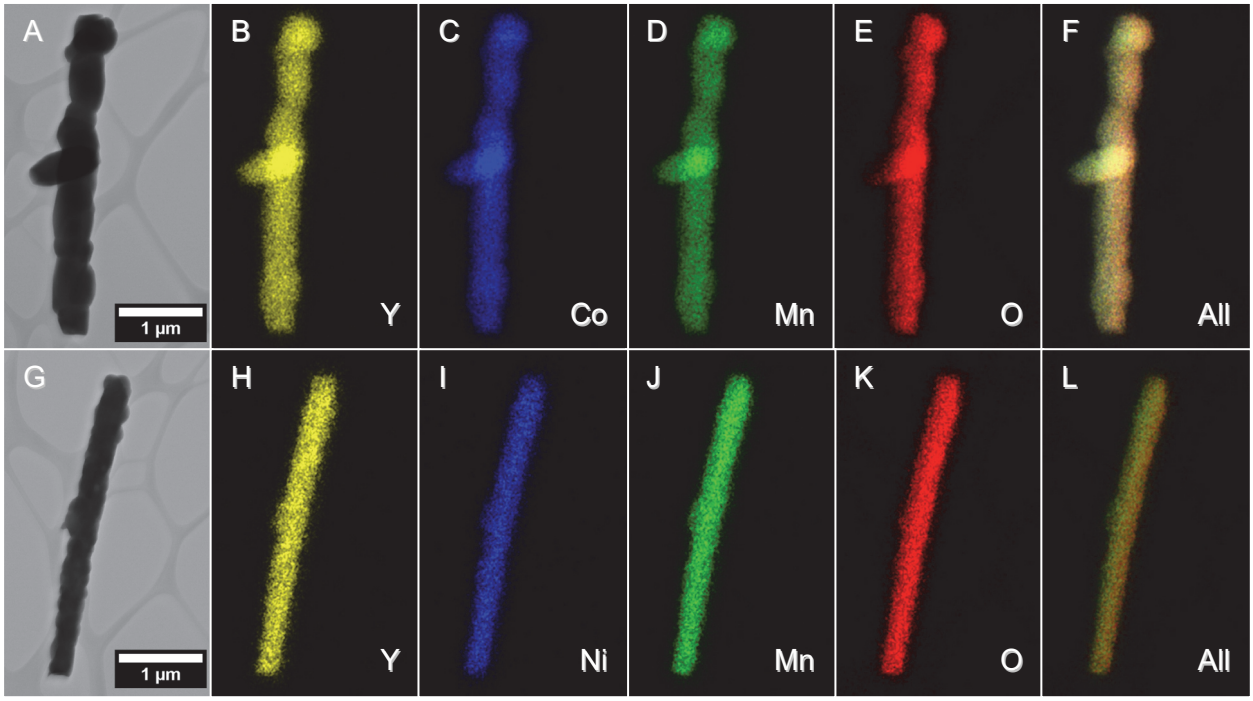

Figure 2. (A, G) STEM images and the (B-F, H-L) EDS mapping data, associated with (A-F) YCMO and (G-L) YNMO.

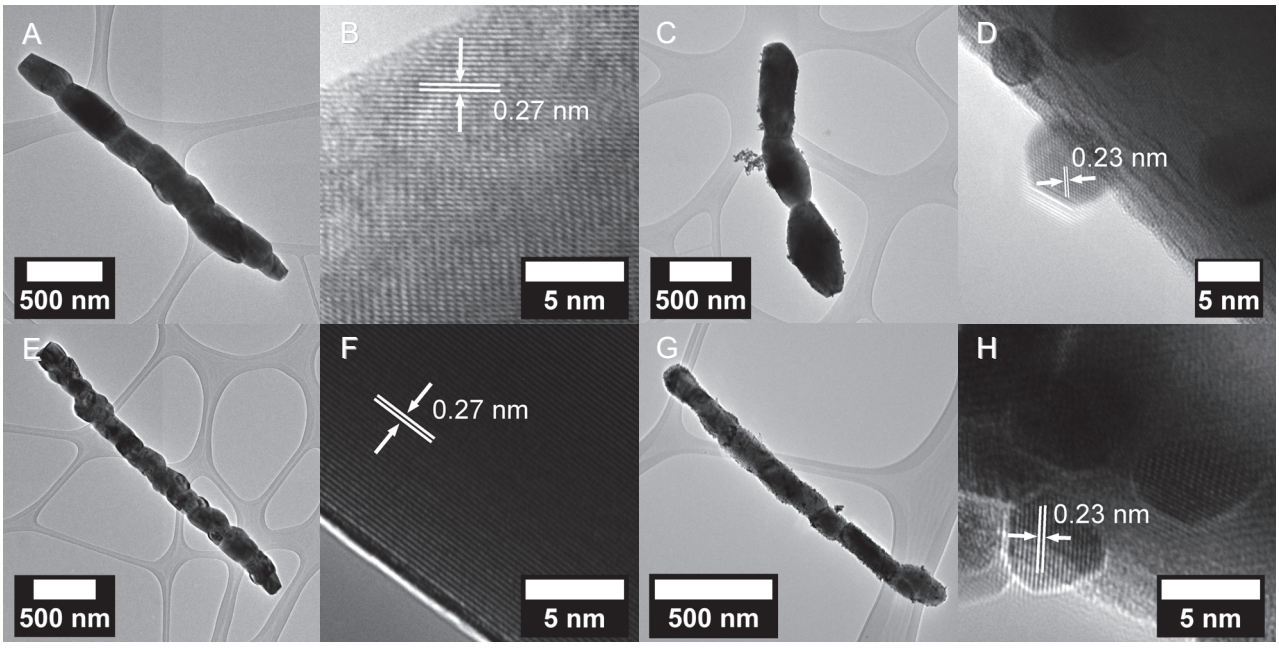

Figure 3. (A, C, E, G) Low-resolution TEM and (B, D, F, H) HRTEM images with the measured *d*-spacings for (A, B) YCMO, (C, D) YCMO/Pt, (E, F) YNMO, and (G, H) YNMO/Pt.

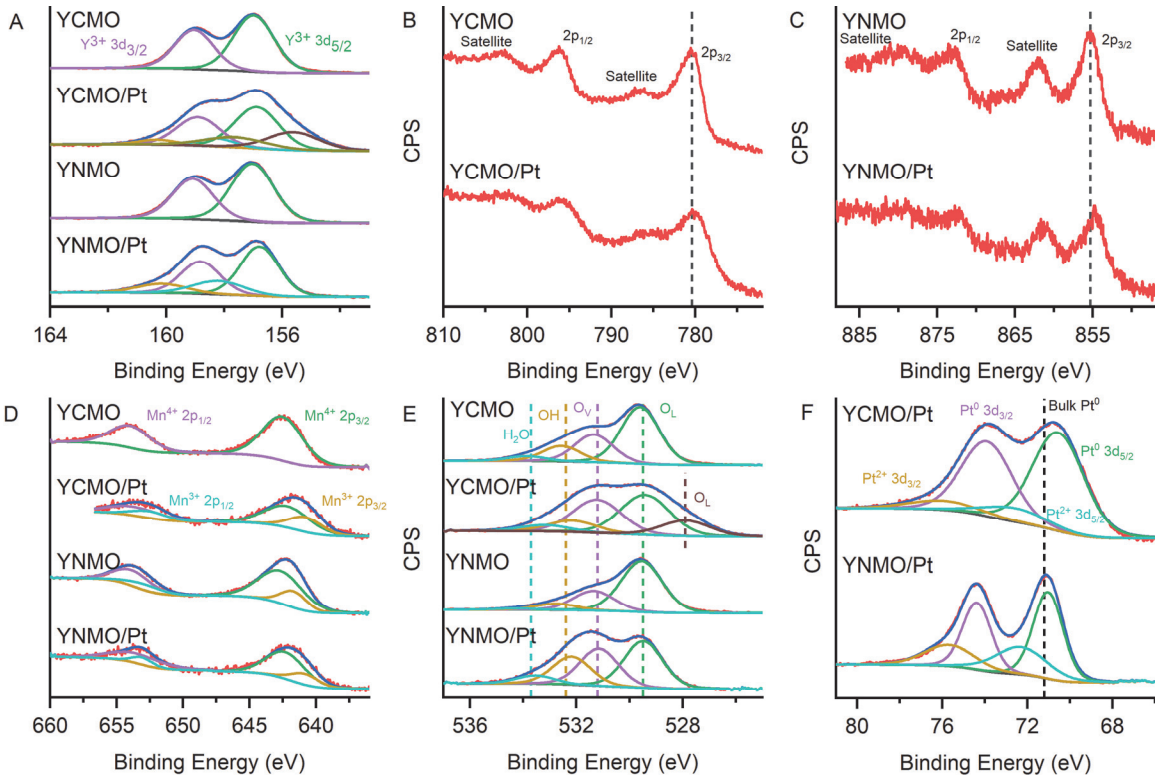

Figure 4. XPS spectra corresponding to the (A) Y 3*d*, (B) Co 2*p*, (C) Ni 2*p*, (D) Mn 2*p*, (E) O 1*s*, and (F) Pt 4*f* regions, respectively.

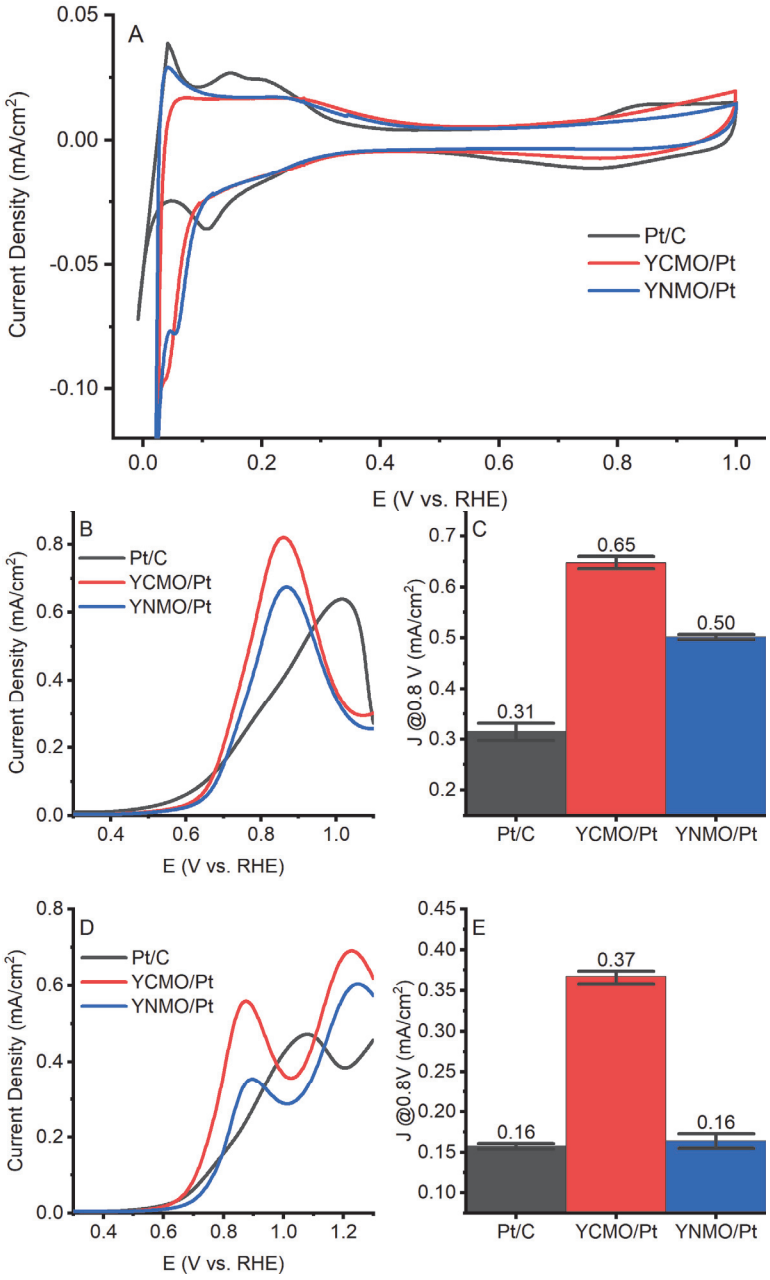

Figure 5. Double Perovskites Used as *Supports* in Alcohol Oxidation Reactions. (A) Representative CV curves of various electrocatalysts collected within an Ar-saturated 0.1 M $HClO_4$ solution. (B) LSV curves for MOR and (C) the corresponding bar graph depict the MOR activity, observed at 0.8 V within an Ar-saturated 0.1 M $HClO_4$ + 0.5 M MeOH solution. (D) LSV curves for EOR and (E) bar graphs display EOR activity at 0.8 V within an Ar-saturated 0.1 M $HClO_4$ + 0.5 M EtOH solution. CVs and LSVs were obtained using a scan rate of 20 mV s^{-1}.

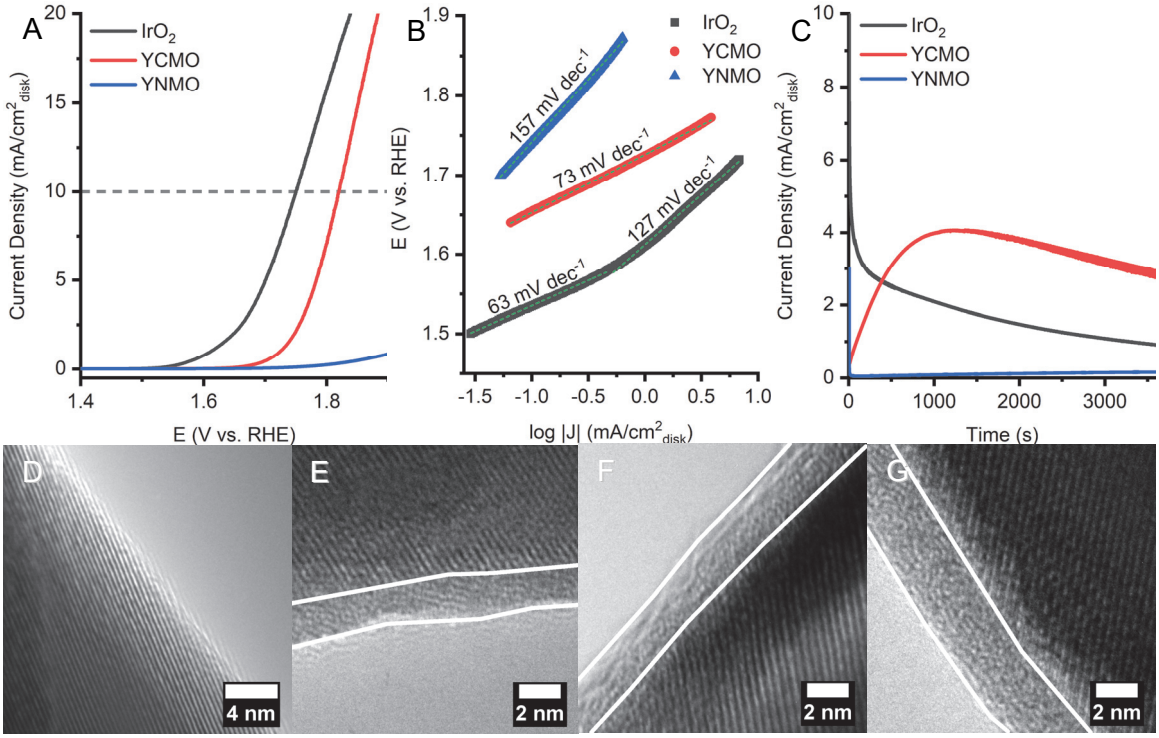

Figure 6. Double Perovskites Used as *Catalysts* in the Oxygen Evolution Reaction. (A) LSV curves of IrO_2, YCMO, and YNMO obtained within an Ar-saturated 0.1 M KOH solution measured with a scan rate of 10 mV/s. (B) Tafel plots highlighting the measured Tafel slopes for IrO_2, YCMO, and YNMO. (C) Chronoamperometry results taken at an overpotential of 500 mV. (D-G) HRTEM images of (D) pristine YCMO and after chronoamperometry measurements, obtained at (E) 5, (F) 20, and (G) 60 min time intervals.

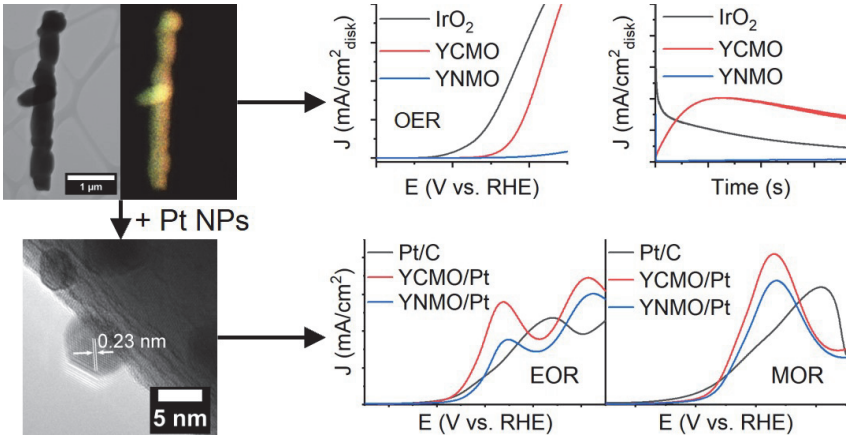

Table of Contents Figure